Combustion and Flame 217 (2020) 248–261

Contents lists available at ScienceDirect

Combustion and Flame

journal homepage: www.elsevier.com/locate/combustflame

Radiation heat transfer in ablating boundary layer combustion theory used for hybrid rocket motor analysis

Kenneth Budzinski, Siddhant S. Aphale, Elektra Katz Ismael, Gabriel Surina III, Paul E. DesJardin*

Department of Mechanical and Aerospace Engineering, University at Buffalo, the State University of New York, Buffalo, NY 14260-4400, USA

ARTICLE INFO

Article history:
Received 4 February 2020
Revised 14 April 2020
Accepted 14 April 2020

Keywords:
Hybrid rocket
Radiation heat transfer
Marxman theory

ABSTRACT

Marxman theory is often used for developing correlations of fuel regression rate for hybrid rocket motor analysis. Effects of radiation are accounted for in this theory as a perturbation to the non-radiating blowing limit allowing for the leading order effects of blowing blockage from radiation heat transfer to influence convective heat flux. The theory does not, however, account for the non-linear changes in radiative gas absorption properties to allow for tightly coupled descriptions of heat transfer and surface blowing. In this study, Marxman theory is expanded in a new fully coupled approach, employing Schvab-Zeldovich coupling functions, unsteady heat transfer response of the fuel, and solution of the gas-phase radiation heat transfer. To develop this theory, Marxman's theory is generalized to allow for expanded functional forms of friction coefficient and account for changes in gas properties. To validate the modeling approach, measurements from a simplified slab burner experiment are conducted. Paraffin wax is used as the fuel and relatively low oxidizer fluxes are employed so the dominate effects of radiation heat transfer can be understood. Measurements of temperature, soot volume fraction, and fuel radiative heat flux rely on two-color pyrometry analyses using high-speed camera color images. Comparisons of model predictions to data indicate the new tightly coupled approach provides good predictions of regression rate, temperature, and radiative heat flux to the fuel surface over the range of oxidizer flow rates considered. Model sensitivity studies reveal commonly used one-way coupling strategies may result in significant over prediction in fuel regression rate that are most likely compensated for by errors in simplified treatments of radiation heat transfer.

1. Introduction

Hybrid rocket motors have been an interesting propulsion paradigm - a potential blend of the benefits of high energy density solid bi-propellant system with the specific impulse of a more traditional liquid fueled air-breathing engine. A hybrid rocket engine works on the principle of the fuel and oxidizer existing in different states, e.g., solid HTPB with liquid oxygen (LOX). Recent reviews on hybrid rocket motors can be found by Sun et al. [1], Komori et al. [2], Naoumov et al. [3], and comprehensive treatise on the topic through 2007 can be found in [4].

One of the challenges of hybrid rockets is defining reliable correlations of fuel regression rate over a range of conditions. Correlations developed in the 1960s, which continue to be used today, rely on the early theories developed by Marxman and co-workers [5–7]. For high oxidizer flow rates, the regression rate can be compactly expressed as: $\rho_s \dot{r} = \dot{m}'' = C_f G B$, where ρ_s is the density of the fuel, $\dot{r}$ is the regression rate, $\dot{m}''$ is the mass flux, C_f is the coefficient of friction, G is the oxidizer flow rate, and B is the blowing rate parameter. While the theory is extremely useful, challenges remain on accounting for the effects of thermal radiation [8]. This issue has resurfaced as recently as in the 2019 study of Leccese et al., where two orders in magnitude difference are reported in grain end-wall radiative heat fluxes between measurements and CFD predictions [9]. The reason for the difference was attributed to the lack of understanding on the role of soot formation in these systems and its substantial effect on overall radiation heat transfer. These observations are consistent with the wide variability of reported soot volume fractions from the literature, ranging from 1 to 100 ppm [9,10]. These studies provide motivation to take a fresh look at how radiation (soot radiation) is accounted for in ablating boundary layer combustion theory.

Historically, the effects of radiation heat transfer on fuel regression rates relied on Marxman et al. where additional block-

* Corresponding author.
E-mail address: ped3@buffalo.edu (P.E. DesJardin).

https://doi.org/10.1016/j.combustflame.2020.04.011
0010-2180/

age of blowing on convection heat transfer is taken into account i.e., one-way coupling of radiation effects on convective blowing [5]. The formulation is presented in terms of a perturbation of the baseline non-radiating case. The result is a correction factor, $F = \dot{q}''_r/\dot{q}''_g + \exp[-\dot{q}''_r/\dot{q}''_g]$, to the baseline fuel regression correlation. Chiaverini et al. expanded on the Marxman correction using data from a HTPB/GOX system where they developed a series of empirically derived correlations [8]. Key contributions of this work included improved Stanton and Nusselt number correlations to account for radiation heat corrections along with a modified blowing number definition. However, the extension of these correlations to other fuel / oxidizer fuel systems is unclear. Furthermore, the changes of additional blowing and boundary layer changes are not coupled back into changes in the gas absorption properties, i.e., two-way coupling. That is, the effects of radiation and surface blowing are not tightly coupled. While more recent computational studies have coupled radiation and surface blowing, they often require assumptions regarding soot volume fraction without a direct connection to measurements [11–13]. Moreover, the computations do not focus on improving existing theoretical estimates of fuel regression rate with radiation that are useful for correlating data.

The objective of this study is to re-examine the early work of Marxman et al. with a focus of developing a tightly coupled formulation for including detailed models of radiation heat transfer [5–7]. The result is a new eigenvalue formulation which includes unsteady heating of the solid fuel and discrete transfer method (DTM) for radiation heat transfer. To validate the improved Marxman model, experiments are carried out in a slab burner configuration, allowing for full optical access to the fuel surface [14]. Simultaneous soot and temperature fields are determined using a DSLR camera based two-color pyrometry [15]. In this approach, the red and green channels from the camera are used to determine soot volume fraction and temperature using an approximate flame hull reconstruction. The flame volume is used to compute the radiative heat flux to the fuel surface using a DTM. Comparisons of gas temperature, fuel regression rates, and surface heat flux indicates the model is able to reproduce many of the observed trends from the experiment over the range of oxidizer flow conditions considered. A key observation from these comparisons is *there is strong feedback from blowing on defining the flame emissivity and view factor - suggesting strongly coupled radiation modeling is necessary for reliable predictions of fuel regression rate.*

The rest of this study is organized as follows. Section 2 presents the semi-analytical model describing regression rates and gas phase combustion properties for 2D slab configuration. Section 3 summarizes the experimental setup and two-color pyrometry diagnostics used for the slab burner. Results and discussion are presented in Section 4 and conclusions are drawn in Section 5.

2. Improved Marxman model for inclusion of radiation heat transfer

2.1. Gas phase

The starting point of Marxman's gas phase analysis begins with the linearized Favre averaged parabolized equations that are used to develop near-wall solutions of the velocity. The local shear stress is approximated as: $\tau(y) = \tau_w + \dot{m}''u(y) = \tau_w(1 + Bu^*)$ with $\dot{m}''$ being the wall normal mass flux, $u^*(= u(y)/u_e)$ is the normalized velocity with y being the wall normal direction. The parameter $B = \dot{m}''u_e/\tau_w = \dot{m}''/(C_f G/2)$ is the blowing rate parameter where u_e denotes the far-field boundary layer velocity [7]. Using Prandtl mixing length model *i.e.*, $\tau(y) = (\mu + \mu_T)\partial u/\partial y$, Marxman cleverly re-expressed the shear stress in terms of blowing and non-blowing contributions, $\partial u^*/\partial\eta = n\eta^{n-1}A(B)(1 + Bu^*)$, where $n \simeq 1/7$ is associated with the assumed velocity profile in the limit as $B \to 0$. As discussed by Lengelle [16], and later analyzed in depth by Karabeyoglu [17], this relation can be analytically integrated to obtain the exact solution,

$$u^*(\eta) = \left[(1 + B)^{\eta^n} - 1\right]/B \tag{1}$$

where $\eta = y/\delta$ is wall normal coordinate normalized by displacement thickness, δ. Using standard boundary layer integral analysis and the assumed blowing profile, the following differential relation is readily derived,

$$\frac{d\delta}{dx} = \frac{C_f}{2}\frac{1 + B}{I} \tag{2}$$

where $I \equiv \int_0^1 u^*(1 - u^*) - \Delta p^* d\eta$, $p^*(= p/(\rho_e u_e^2))$ is the normalized pressure and $C_f(= \tau_w/\rho u_e^2)$ is the coefficient of drag. Assuming small stream-wise pressure gradient, $I(B)$ can be numerically integrated and stored as a function of B, or further can be linearized so an explicit analytical expression determined such as those developed by Marxman, *i.e.*, $I = 7[1 + 13B/10 + 4B^2/11]/(72(1 + B/2)^2)$ [7]. Re-expressing Eq. (2) as:

$$\frac{d\delta}{dx} = \frac{C_{f,o}(x)}{2}\left(\frac{C_f}{C_{f,o}}\right)\frac{1 + B}{I} \tag{3}$$

then the effects of B from downstream x can be separated out where $C_{f,o}(x)$ corresponding to the $B \to 0$ limit and $C_f/C_{f,o}$ is only a function of B. Marxman linearized the u^* profile resulting in $C_f/C_{f,o} = \ln(1 + B)/B$ where $0 < B < 100$ [7]. Later Lengelle refined this analysis resulting in [16],

$$C_f/C_{f,o} = [1 + 1/2(1 - \exp(-0.05B))]\frac{ln(1 + B)}{B}. \tag{4}$$

An extensive analysis and review of these assumptions is given by Karabeyoglu [17]. In this study, the result from Lengelle given in Eq. (4) is used. Assuming $C_{f,o}(x) = 0.0225Re_\delta^{-1/4}$ then Eq. (3) can be analytically integrated to provide the final form of the displacement thickness.

$$\delta(x) = \left[(0.0225)\frac{5}{8}\frac{C_f}{C_{f,o}}\frac{1 + B}{I}\right]^{4/5} Re_x^{-1/5}x. \tag{5}$$

To couple momentum boundary layer analysis to gas phase combustion processes, Shvab–Zeldovich coupling functions are defined in terms of enthalpy and oxidizer ($h - OX$), fuel-oxidizer ($f - ox$) and mixture fraction (Z). The usual assumptions apply with this analysis, *i.e.*, Chapman gas, unity Lewis number, *etc.* Using transport equations coupling functions can be defined for a *non-radiating* flow,

$$b_{f-ox} = \frac{Y_{ox}(y)/\nu_{ox} + Y_{f,s} - Y_f(y)}{Y_{ox,e}/\nu_{ox} + Y_{f,s}} \tag{6a}$$

$$b_{h-ox} = \frac{(\Delta h_c/\nu_{ox})Y_{ox}(y) + h(y) - h_s}{(\Delta h_c/\nu_{ox})Y_{ox,e} + h_e - h_s} \tag{6b}$$

$$b_Z = 1 - Z(y)/Z_s \tag{6c}$$

where subscripts s and e denote fuel surface and far-field boundary layer edge properties, Δh_c is the heat of combustion and h is the sensible enthalpy. Note, $Y_{ox,s} = Y_{f,e} = 0$ is assumed in the coupling function definitions. Assuming a Reynolds analogy then $db_{h-ox}/d\eta = du^*/d\eta = \rho_e u_e \delta C_f/(2\mu)$ which can be re-arranged to determine the heat flux to the surface.

$$\dot{q}''_g = \frac{GC_f}{2Pr_g}[(\Delta h_c/\nu_{ox})Y_{ox,e} + h_e - h_s] \tag{7}$$

It should be emphasized that the implicit assumption in defining coupling functions involving enthalpy and Reynolds analogy is the transport of energy (enthalpy) is dynamically similar to mass and

momentum transport. For weakly radiating thin flames, this assumption is reasonable since reactions are diffusion controlled and chemistry source/sink terms associated with energy transport differ from species by a proportionality constant associated with stoichiometry (assuming simple chemistry). However, for strongly radiating flames, dynamic similarity is no longer the case, and therefore the use of a Reynolds analogy falls on a weaker foundation.

Marxman et al.'s extension of the formulation to include the effects of radiation *assumes* the regression follows the same functional form as the non-radiation case [6],

$$\dot{m}'' = \frac{C_{f,o}}{2}\frac{C_f}{C_{f,o}}GB_* \simeq \frac{C_{f,o}}{2}GB_*^{0.23} \tag{8}$$

where B_* corresponds to the blowing factor with the effects of thermal radiation. The second equality in Eq. (8) comes from the simplification, $C_f/C_{f,o} \simeq 1.2B^{-0.77}$ [6]. Using these simplification and balancing energy across the fuel-gas interface, Marxman et al. derived the following relation,

$$\frac{B_*}{B} = 1 + \frac{\dot{q}''_{rad}}{\dot{q}''_g}\left(\frac{B_*}{B}\right)^{0.77} \tag{9}$$

which can be approximated as: $B_*/B \simeq \exp(1.3\,\dot{q}''_{rad}/\dot{q}''_g)$. Substituting this relation back into Eq. (8), a modified regression rate that accounts for enhanced blowing is derived [6].

$$\dot{m}'' = \frac{\dot{q}''_g}{L'_v}\left[\frac{\dot{q}''_{rad}}{\dot{q}''_g} + \exp\left(-\frac{\dot{q}''_{rad}}{\dot{q}''_g}\right)\right] = \frac{\dot{q}''_g}{L'_v}F(\dot{q}''_{rad}/\dot{q}''_g) \tag{10}$$

where L'_v is the effective latent heat of vaporization and the function F may be viewed as a radiative correction factor. Adaptations of this approach include the study of Chiaverini et al. where the basic Marxman framework is maintained and augmented with experimentally obtained empirical constants that are fuel system specific, *i.e.*, $F = c(\dot{q}''_{rad}/\dot{q}''_g)^d + \exp[-c(\dot{q}''_{rad}/\dot{q}''_g)^d]$, where c and d are constants which result in the best agreement to their fuel regression rate data [8]. They also propose a slight deviation of the modified transfer number, $B_* = B\exp[n\exp(\dot{q}''_{rad}/\dot{q}''_g)]$, where B has the same transfer number from the classical Marxman theory and $n = 1.0$. The appeal of this theory and variants thereof, is it explicitly accounts for the the leading order effects of additional blowing and associated blockage. However, it does not couple these changes back into changes to flame emissivity and view factor. This is most likely due to the historical use of relatively simple radiation heat transfer models.

In this study, a more tightly coupled solution approach is pursued. The starting point of the analysis is to first express the combustion and radiation source term in the enthalpy transport (assuming simple chemistry) as:

$$-\dot{m}'''_F\Delta h_c - \kappa_P(\sigma T^4 - G) = -\dot{m}'''_F\Delta h_c(1-\chi_r) = -\dot{m}'''_F\Delta h'_c \tag{11}$$

where $\dot{m}'''_F < 0$ is the fuel consumption rate, $G = \int_{4\pi} Id\Omega$ is the local irradiation, and κ_P is the Planck mean absorption coefficient. The quantity, $\chi_r = \kappa_P(\sigma T^4 - G)/\Delta h_c$, is defined as the net radiative emission fraction and is assumed constant. For most of the hydrocarbon flames, $\chi_r \simeq 0.3$ [18]. Under these assumptions, a Reynolds analogy can be safely assumed and equivalent coupling functions to those given in Eq. (6) may be derived with Δh_c replaced with an effective heat of combustion, $\Delta h'_c$. Effects of radiation can therefore be imposed directly in the solution to the eigenvalue problem for the mass blowing rate,

$$B_* = \frac{\dot{m}''u_e}{\tau_w} = \frac{2\dot{m}''}{C_{f,*}G} = \frac{Y_{f,s}+Y_{ox,e}/\nu_{ox}}{1-Y_{f,s}} = \frac{(\Delta h'_c/\nu_{ox})Y_{ox,e}+h_e-h_s}{L'_v}$$
$$= \frac{(\Delta h'_c/\nu_{ox})Y_{ox,e}+h_e-h_s+2Pr_{g,*}(\dot{q}''_{rad}-\dot{q}''_{l,lg})/(C_{f,*}G)}{Pr_{g,*}L_v} \tag{12}$$

where the subscript * indicates quantities that change when radiation is taken into account. The last equality is defined by substituting in for the effective latent heat of vaporization, $L'_v \equiv Pr_g(L_v + \dot{q}''_{l,lg}/\dot{m}'' - \dot{q}''_{rad}/\dot{m}'')$, where $\dot{q}''_{rad} = \epsilon_w(\int_{2\pi} I(\hat{s})\hat{n}\cdot\hat{s}d\Omega - \sigma T_{ls}^4)$ is the *net* radiative heat flux at the fuel liquid-gas surface assuming the absorptivity and emissivity are equal. The incident radiative intensity, $\dot{q}''_{rad,inc} = \int_{2\pi} I(\hat{s})\hat{n}\cdot\hat{s}d\Omega$, required for $\dot{q}''_{rad}$ is calculated using a DTM, to be discussed in Section 2.3.

Assuming the liquid-vapor fuel interface is at saturation conditions then an Antoine equation of state may be used to relate the vapor partial pressure to temperature,

$$P_v(T) = A - B/(C + T_s) \tag{13}$$

where the constants $A = 7.1356,\ B = 2276.9,\ C = 75.9$ are taken from [19] (temperature in C and pressure in PSI). If $\dot{q}''_{l,lg}$ is assumed equal to zero then Eqs. (12) and (13) represent four coupled nonlinear equations for solution of the $\dot{m}''$, T_s, $Y_{f,s}$ and B at each downstream location along the fuel surface. However, to close the system of equations two additional quantities are required. The first is the heat transfer into the liquid and solid phases that will be discussed in Section 2.2. The second is the evaluation of C_{f^*} which is required in Eq. (12). This quantity may be expressed as:

$$C_{f,*} = C_{f,o}\left(\frac{C_f}{C_{f,o}}\right)\left(\frac{C_{f,*}}{C_f}\right) \tag{14}$$

where $C_f/C_{f,o}$ represents the perturbation of C_f due to blowing and *without* radiation. The ratio $C_{f,*}/C_f$ represents changes in blowing *with* the effects of radiation (vs. without it). While numerous approximations have been developed to define $C_f/C_{f,o}$, defining $C_{f,*}/C_f$ is much less clear. As discussed by Marxman et al., radiation leads to additional blowing and therefore greatly reduces C_f from the reduction in velocity gradients [5]. To better illuminate this relationship, Eqs. (7) and (12) are used to construct B_*/B :

$$\frac{B_*}{B} = \frac{Pr_g}{Pr_{g*}}\left[1 - \frac{\chi_r(\Delta h_c/\nu_{ox})Y_{ox,e}}{(\Delta h_c/\nu_{ox})Y_{ox,e}+h_e-h_s}\right]$$
$$+\frac{\dot{q}''_r}{\dot{q}''_g}\left(\frac{C_{f*}}{C_f}\right)^{-1} \simeq \frac{Pr_g}{Pr_{g*}} + \frac{\dot{q}''_r}{\dot{q}''_g}\left(\frac{C_{f*}}{C_f}\right)^{-1} \tag{15}$$

where it is assumed h_s is the same with or without radiation since the liquid will be most likely near boiling in either case. The second equality assumes χ_r is sufficiently small such that the term in square brackets is near unity. Eq. (15) is a generalization of Marxman's original relation given in Eq. (9) and highlights the important direct relationship between changes in the blowing number with changes in C_f. As first introduced by Marxman, if the functional forms of C_f and C_{f^*} are *assumed* to be the same, then Eq. (15) defines an implicit relation for determining B_*/B in terms of $\dot{q}''_r/\dot{q}''_g$. Once B_*/B is known then the corresponding $C_{f,*}/C_f$ can be computed. Figure 1 shows B_*/B and $C_{f,*}/C_f$ using several functional $C_f/C_{f,o}$ model forms. "Marxman empirical" refers to the solution of Eq. (9) using numerical methods. "Marxman Fit" refers the fit by Marxman et al. to the solution of Eq. (9), $B_*/B = \exp(1.3\dot{q}''_r/\dot{q}''_g)$, that is commonly used in the literature [6]. The Lengelle solution refers to the solution to Eq. (15) using Eq. (4) for $C_f/C_{f,o}$. As shown, a wide variation in C_{f^*}/C_f is observed depending on which model of $C_f/C_{f,o}$ is selected, suggesting the regression rate will be highly sensitive to corrections for radiation. It should be noted that assuming C_{f^*} and C_f have the same functional form is non-unique and expected to lead to erroneous results for large values of $\dot{q}''_r/\dot{q}''_g$. In fact, inspection of B_* with increasing $\dot{q}''_r/\dot{q}''_g$ shows B_* exceeds 100 for $\dot{q}''_r/\dot{q}''_g > 3.02$, *i.e.*, values of B_* outside the range of applicability. The 3.02 threshold is remarkably close to the threshold of 2.86 for HTPB reported by Chiaverini et al. [8] where large deviations are observed between Marxman's correlation and their empirical corrections. This finding suggests the Marxman assumption of similar

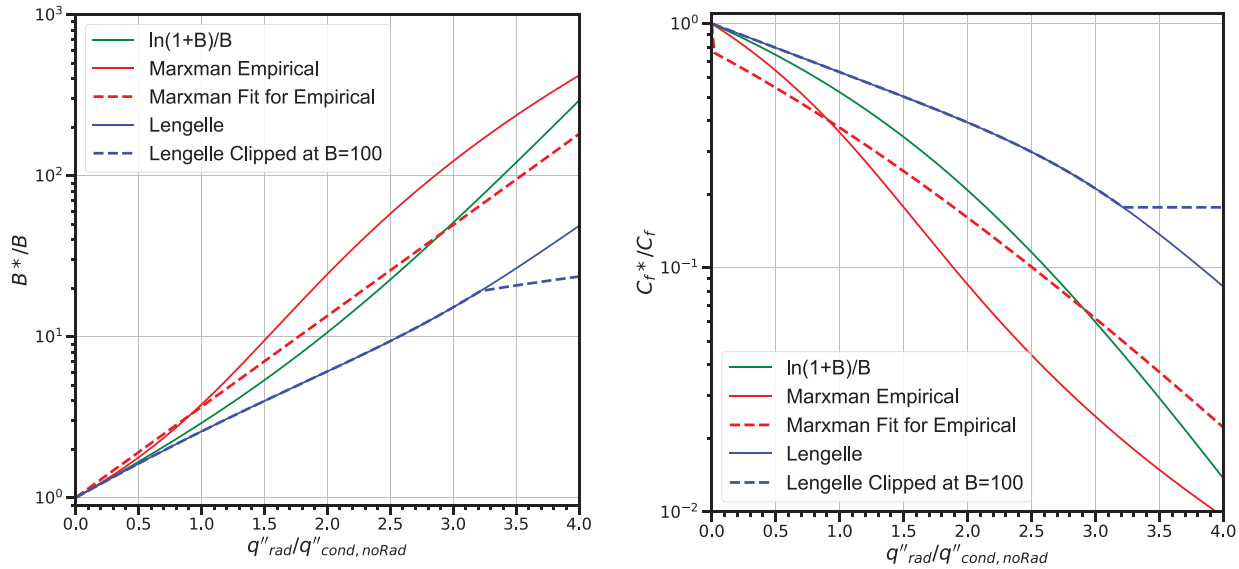

Fig. 1. Effects of radiation on blowing factor and coefficient of friction showing (a) B_*/B and (b) C_{f^*}/C_f.

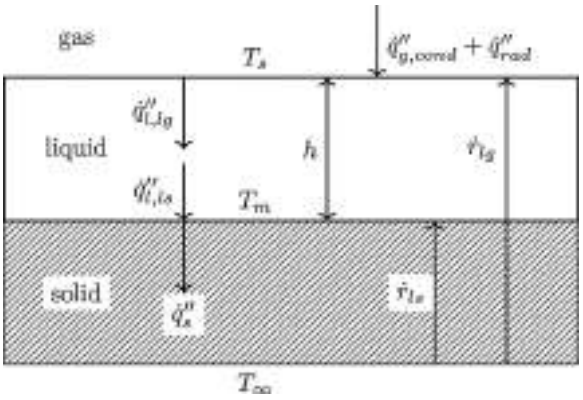

Fig. 2. Sketch of fuel liquid and solid phase heat transfer model.

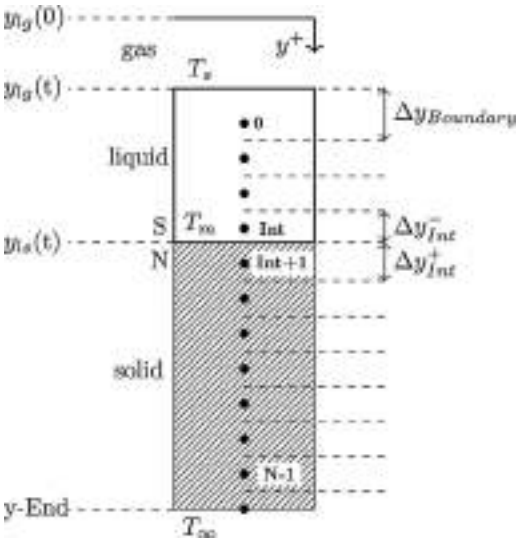

Fig. 3. The FV discretization used in the numerical model.

functional forms for C_f breaks down for $B_* > 100$. A correction is therefore proposed to clip C_{f^*}/C_f for $B_* > 100$. The clipped version is also presented in Fig. 1 using the Lengelle correlation, but the clipping could easily be implemented to any of the existing $C_f/C_{f,o}$ correlations. For the purposes of making comparison to experimental measurements, only the Lengelle and Lengelle clipped correlations are used.

2.2. Heat transfer model of liquid / Solid phases

Figure 2 shows the heat transfer solution space of interest showing the liquid and solid phases of the fuel. Models describing heating and melt front progression often rely on analytical solutions that assume regression rates at liquid-gas and solid-liquid interface are equal, *i.e.*, $\dot{r}_{lg} = \dot{r}_{ls}$ [17]. This assumption is acceptable for high heat fluxes but invalid for low heating rates, as detailed in A.2.

To avoid making this assumption, a one-dimensional finite volume (FV) description of the liquid and solid phases is developed and shown in Fig. 3, where the $\dot{r}_{lg} = \dot{r}_{ls}$ assumption is relaxed.

The FV formulation starts with the unsteady convection-diffusion equation,

$$\frac{\partial T}{\partial t} + v_k \frac{\partial T}{\partial y} = \alpha_k \frac{\partial^2 T}{\partial y^2} \tag{16}$$

to be discretized and solved, where $k = \{s, l\}$ represents either the solid or liquid phase velocity. For the solid phase, $v_s = 0$. For the liquid phase, the velocity accounts for the density difference between the solid and liquid phases. If the liquid phase is assumed incompressible then the liquid velocity is constant along the through thickness and from mass conservation, $v_l = \dot{r}_{ls}(\rho_s/\rho_l - 1)$.

For the interior nodes, Eq. (16) is discretized as:

$$T_i^{n+1} - T_i^n = T_{i-1}(D + C/2) + T_i(-2D) + T_{i+1}(D - C/2), \tag{17}$$

where a fixed grid is used, $C/2 = v_k \Delta t/(2\Delta y)$, and $D = \Delta t \alpha/\Delta y^2$. Here α_k, is the thermal diffusivity. A theta method is used on Eq. (17) to step the solution in time leading to the linear system,

$$\begin{aligned} &T_{i-1}^{n+1}(-\theta(D + C/2)) + T_i^{n+1}(1 + 2\theta D) + T_{i+1}^{n+1}(-\theta(D - C/2)) \\ &= T_{i-1}^n(1-\theta)(D + C/2) + T_i^n(1 - (1-\theta)2D)) \\ &+ T_{i-1}^n(1-\theta)(D - C/2), \end{aligned} \tag{18}$$

needed to be solved for the solution at the next time step. The complete problem is split into two stages, the first stage is the pre-

heating of the solid to the melting temperature. Since the coupling is a local formulation in x, the immediate upstream heat flux is estimated using the adiabatic heat flux defined by,

$$\dot{q}''_{g,ad} = L_v \dot{m}'' = L_v C_f G B_* / 2, \tag{19}$$

where only the solid phase heating is considered. At $y = 0$ the adiabatic heat flux is applied, leading to the following constraint for the discrete equation.

$$T_0^{n+1}(1 + 2\theta D) + T_1^{n+1}(-2\theta D) = \frac{2\dot{q}''_{g,ad}\Delta t}{\rho C_s \Delta Y} + T_0^n(1 - (1-\theta)2D) + T_1^n(1-\theta)2D \tag{20}$$

Eqs. (18), (20), and a homogeneous Neumann condition on the lower boundary describe the preheating stage.

The second stage involves the liquid and solid phases as well as a moving boundary and phase interface. Here the domain is split into two at the liquid-solid interface which is kept at the melting temperature of the paraffin wax. Above the interface, ($y > y_{Int}$), is the solid region that is initially preheated. Below the interface is the liquid region of paraffin wax. Both of the interior cells in each domain can be discretized by Eq. (18) using the correct velocities and phase properties. The boundary conditions at the liquid-solid interface are defined using time changing control volumes. At a given time step, the node below the interface is defined as the interface node (Int). The control volume for this node extends from south face of the interface down to the end of the previous control volume, as seen in Fig. 3. The heat flux at the south part of the liquid/solid interface (S) is approximated as: $\dot{q}''_{ls,S} = -k_l(T_m - (T_{Int} + T_{Int-1})/2)/(y_{ls} - (y_{Int} - \Delta y/2)) = -k_l(T_m - (T_{Int} + T_{Int-1})/2)/\Delta y^-_{Int}$ resulting in the following discrete equation for the interface node.

$$\begin{aligned}
&T_{Int}^{n+1}\left[1 - \frac{\theta\Delta t}{\Delta y^-_{Int}}\left(\frac{v_l}{2} - \frac{\alpha_l}{2\Delta y^-_{Int}} - \frac{\alpha_l}{\Delta y}\right)\right] \\
&\quad + T_{Int-1}^{n+1}\left[-\frac{\theta\Delta t}{\Delta y^-_{Int}}\left(\frac{v_l}{2} - \frac{\alpha_l}{2\Delta y^-_{Int}} + \frac{\alpha_l}{\Delta y}\right)\right] \\
&= T_{Int}^{n}\left[1 + \frac{(1-\theta)\Delta t}{\Delta y^-_{Int}}\left(\frac{v_l}{2} - \frac{\alpha_l}{2\Delta y^-_{Int}} - \frac{\alpha_l}{\Delta y}\right)\right] \\
&\quad + T_{Int-1}^{n}\left[\frac{(1-\theta)\Delta t}{\Delta y^-_{Int}}\left(\frac{v_l}{2} - \frac{\alpha_l}{2\Delta y^-_{Int}} + \frac{\alpha_l}{\Delta y}\right)\right] \\
&\quad + T_m\frac{\Delta t}{\Delta y^-_{Int}}\left(\frac{\alpha_l}{\Delta y^-_{Int}} - v_l\right)
\end{aligned} \tag{21}$$

A similar approximation is employed for the node above the interface, resulting in the following for node $Int + 1$,

$$\begin{aligned}
&T_{Int+1}^{n+1}\left[1 + \frac{\theta\alpha_s\Delta t}{\Delta y^+_{Int}}\left(\frac{1}{2\Delta y^+_{Int}} + \frac{1}{\Delta y}\right)\right] \\
&\quad + T_{Int+2}^{n+1}\left[\frac{\theta\alpha_s\Delta t}{\Delta y^+_{Int}}\left(\frac{1}{2\Delta y^+_{Int}} - \frac{1}{\Delta y}\right)\right] \\
&= T_{Int+1}^{n}\left[1 - \frac{(1-\theta)\alpha_s\Delta t}{\Delta y^+_{Int}}\left(\frac{1}{2\Delta y^+_{Int}} + \frac{1}{\Delta y}\right)\right] \\
&\quad + T_{Int+2}^{n}\left[-\frac{(1-\theta)\alpha_s\Delta t}{\Delta y^+_{Int}}\left(\frac{1}{2\Delta y^+_{Int}} - \frac{1}{\Delta y}\right)\right] + T_m\frac{\alpha_s\Delta t}{{\Delta y^+_{Int}}^2},
\end{aligned} \tag{22}$$

where $\Delta y^+_{Int} = y_{Int+1} - y_{ls} + \Delta y/2$ is the length of the control volume above the interface, as seen in Fig. 3.

The moving melt interface is tracked using the Stefan condition and by approximating the conductive heat flux above and below the interface using the method introduced above,

$$\dot{r}_{ls} = \frac{\dot{q}''_{ls,S} - \dot{q}''_{ls,N}}{\rho_s L_m}. \tag{23}$$

The top boundary of the liquid layer is coupled with the gas phase analytics and the gas-liquid interface Stefan condition to obtain the top boundary equation for the liquid phase and to move the liquid-gas boundary. The radiative heat flux is calculated using a ray tracing algorithm throughout the gas phase which is then added to the conductive surface heat flux given by Eq. (7) to obtain the total heat flux from the gas at the boundary. The Stefan condition at the gas-liquid interface is then defined by,

$$\dot{r}_{lg} = v_l + \frac{\dot{q}''_{g,cond} + \dot{q}''_{rad} + k_l\frac{\partial T}{\partial y}|_{y=0}}{\rho_l L_v}. \tag{24}$$

With radiation involved, there is a nested iterative solver. The overall coupling algorithm of the solid/liquid phase heat transfer model with the gas phase is summarized in Appendix A, along with model validation examples.

2.3. Radiation model

A 3D ray-tracing based radiative heat transfer model is used to compute the radiative heat flux to the fuel surface [9,10,15,20]. Rays are first traced out from the surface through the flame hull. The flame hull is constructed either experimentally using the two-color pyrometry field information [15], or numerically using the local gas-phase solutions. In either case, the flame is assumed homogeneous in the cross-steam direction and equal to the width of the wax sample. Rays are then integrated backwards to determine the local intensity at the fuel surface using the local analytical solution,

$$I_{\hat{s},k+1} = I_{\hat{s},k}\exp(-\kappa_k\Delta l_{\hat{s},k}) + I_{b,k}\epsilon_k, \tag{25}$$

where $\hat{s}$ is the directional vector of the ray from the point on the surface, κ_k and ϵ_k are the absorption coefficient and emissivity, respectively, at the k^{th} point on the ray, and $\Delta l_{\hat{s},k}$ is the spatial step size of the ray at point k. $I_{b,k}$ and $I_{\hat{s},k}$ are the black body intensity and ray intensity evaluated at the temperature at the k^{th} point of the ray along the direction $\hat{s}$ respectively. The heat flux at the surface is evaluated by,

$$\dot{q}''_{rad} = \sum_{i=1}^{N_a}\sum_{j=1}^{N_p} I_{\hat{s},N_r}\cos(\theta_j)\sin(\theta_j)\Delta\theta\Delta\phi. \tag{26}$$

where $\Delta\theta = \Delta\phi = 3^o$ resulting in 3,800 rays to determine the heat flux. As will be shown, the radiation is dominated by soot with gas phase emission from water vapor and carbon dioxide contributing little. Gas emissivity is computed using empirical relation given in [21]. The Planck mean absorption coefficient is assumed to follow [22],

$$\kappa(T, f_v) = 3.60 f_v C_0 T / C_2. \tag{27}$$

The emissivity is then given by, $\epsilon_k = 1 - \exp(-\kappa_k\Delta l_{\hat{s},k})$. For model predictions, the soot volume fraction is assumed constant and set equal to mean soot volume fraction measurements using two-color pyrometry ranging from 54 ppm (high G) to 60 ppm (low G), as will be discussed in 3.3.

3. Experimental setup and diagnostics

3.1. Slab burner setup

The experimental apparatus follows closely that developed by Dunn et al. [14]. Figure 4 shows the setup consisting of two stainless steel plates with pieces of heat resistant borosilicate glass. The slab burner's dimensions are 15.24 cm long by 2.54 cm height. The chamber is fed by a 2.54 cm inner diameter stainless steel pipe. The length of the pipe is 1.83 m consistent to that in [14]. No flow conditioning is used. The pipe Reynolds number is in the range of

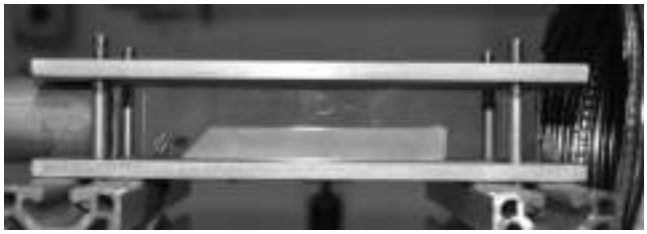

Fig. 4. The slab burner setup.

Fig. 5. Nikon camera DSLR images showing (a) raw and (b) processed binary image using masking.

7300–27,500 for the mass flux range studied and is well beyond the critical Reynolds number of 2300. Based on the hydrodynamic entrance length calculation the flow at the exit of the pipe, entering the chamber is fully developed. The distance between the side glasses and top and bottom steel plates is 2.54 cm, the same distance as the internal diameter of the circular pipe.

An Omega FMA 1744a mass flowmeter is used to measure the mass flux of the solenoid controlled oxygen and air. The flowmeter can measure in a range of 5 - 500 SLMs, with an accuracy of ± 1.5%. The paraffin wax is ignited using a ethylene vinyl acetate (EVA) attached to nickel chromium (nichrome) igniter wire with steel wool for the pyrogen, as is suggested by Dunn et al. [14]. The system is automated using relays to activate the ignition and solenoid valves. Lab grade paraffin wax (Carolina Biological Supply) is used with a melting point of 320 – 327 K. The paraffin samples are formed in a mold and slowly cooled to room temperature. The dimensions of the samples are 9.36 – 9.56 mm wide, 10 – 11.4 mm high, and 70 – 100 mm, long with a 45° chamfer at the front face to promote flame attachment (see Fig. 5). The oxidizer inflow is at 298 K.

3.2. Fuel regression rates

An Edgertronic SC-1 high-speed camera is used to capture burn characteristics and perform two-color pyrometry [15]. Regression rates are measured using a Nikon DSLR camera with a high-intensity flash. The camera is triggered in burst mode to capture about 40 images during the 12 *s* experimental run-time. For each image, a binary mask is constructed and monitored to infer local and global regression rates, as illustrated in Fig. 5.

Experimental regression rates are computed from the wax images captured using the high intensity flash assisted DSLR camera. A MATLAB script is used to manually trace the boundary of the wax in each image. Based on the traced boundary the images are converted into binary form as shown in Fig. 5. The change in the height of the top surface of the wax is tracked in all the images and an external stop watch data is used to calculate the regression rates. The height of the wax is tracked over time and fit using a cubic polynomial curve and its derivative used to determine regression rate, as shown in Fig. 6 for a single location. Similarly, all the locations on the wax for all the oxidizer flux are fitted to obtain the temporally and spatially resolved regression rates for increasing oxidizer flow rate.

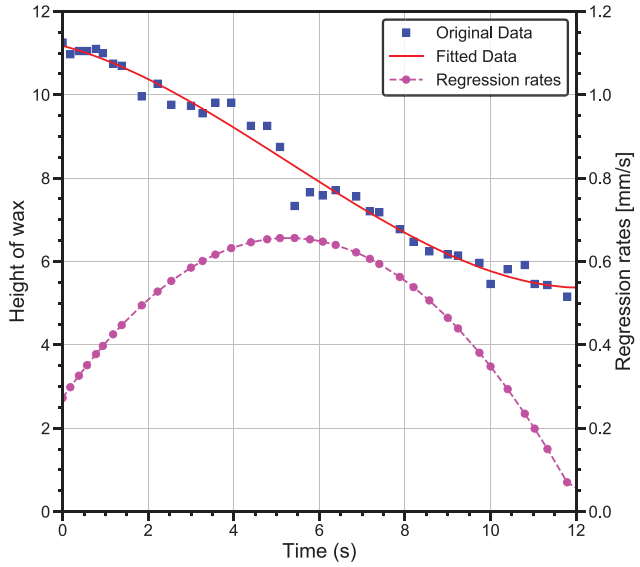

Fig. 6. Curve fit of fuel regression rate at a single location for $G = 5.91\ \mathrm{kg/m^2} - s$.

3.3. Two-color Ppyrometry

Two-color pyrometry has enabled researchers to accurately measure temperatures of flames non-intrusively using a CCD or CMOS based digital cameras [15]. The measurement relies on the ratio of two intensities at different wavelengths using Wien's approximation to Planck's law. While previous studies that have measured gas temperature, used emission spectroscopy from paraffin wax/GOX systems, they often assume a black body emitter [9,23,24], even though soot emits inversely proportional to wavelength [22,25]. For this study, the two-color pyrometry methodology developed by Aphale and DesJardin [15] is adopted where Edgertronic high-speed camera is used to determine gas temperature and soot volume fraction using an approximate flame hull reconstruction. The fuel surface radiative heat flux can then be determined using a ray tracing algorithm. The temperature of the flame is determined using the following,

$$T = \frac{C_2(1/\lambda_R - 1/\lambda_G)}{\ln\left(\frac{I_{G,\bar{s},k}}{I_{R,\bar{s},k}}\right) + \ln\left(\frac{\varepsilon_\lambda(\lambda_G)}{\varepsilon_\lambda(\lambda_R)}\right) + \ln\left(\frac{\lambda_G}{\lambda_R}\right)^5 + \ln\left(\frac{c_{\lambda,R}}{c_{\lambda,G}}\right)} \tag{28}$$

where, $C_2 = hc/k_b = 14388.8\ \mu\mathrm{m} \cdot K$ is the second Planck's constant, with h being the Planck's constant, c is the speed of light, k_b is the Boltzmann constant, $\lambda_R = 650$ nm is the red narrow wavelength, and $\lambda_G = 532$ nm is the green narrow wavelength, I_R and I_G are the red and green intensities, respectively, ε_λ is the soot emissivity at a given wavelength, and $c_{\lambda,R}$ and $c_{\lambda,G}$ are the calibration constants associated with the camera [15].

The Edgertronic camera is radiometrically calibrated to obtain the mapping between the digital pixel intensities and the physical source intensity using a NIST traceable calibrated tungsten filament lamp (StellarNet Inc.). Figure 7 shows the Edgertronic high-speed camera response function obtained using the calibration technique described in [15]. The camera response is approximately linear for the pixel intensities in the range of 20 – 200. It is desirable to obtain the camera signal in this pixel intensity range. To prevent camera over-saturation from the bright flame, an Edmund Optics neutral density filter (ND) is used with 0.3 optical density (OD). The neutral density filter allows only 50% transmission and is also accounted while calibration. To account for the combustion chamber glass optical aberrations, the calibration technique from [15] is modified by placing the glass in between the calibration lamp and the camera and the use of ND filter. Since the Edgertronic camera

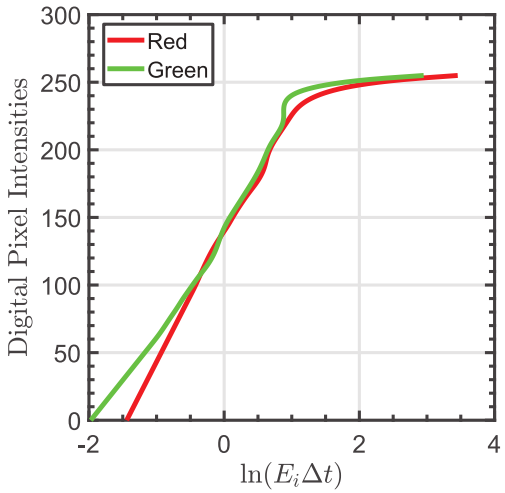

Fig. 7. Edgertronic high-speed camera calibration response function.

does not provide RAW video data, images are extracted from the video and stored using 8-bit encoding.

The flame hull is determined by assuming flame properties are homogeneous in the cross-stream direction over the width of the wax, (l_f). The soot volume fraction (f_v) is computed using the intensity from the red channel and the gas temperature measured using [15],

$$f_v = \frac{-\lambda}{C_{0,\lambda} l_f} \ln\left[1 - \frac{I_\lambda \lambda^5 (\exp(C_2/\lambda T) - 1)}{C_1}\right] \tag{29}$$

where, $C_1 = 2\pi hc^2 = 3.7418 \times 10^{-16}\ W \cdot m^2$ is Planck's first constant. The computed flame temperature and soot volume fraction is then used to obtain the flame to fuel radiative heat flux using a ray tracing algorithm as described in [15]. The high speed camera is set to capture the combustion at 4000 frames per second (FPS) and the shutter speed is 100 μs. The capture time is set to 12 s. Depending on the oxidizer flux the experiment runs from $5\,s - 8\,s$ which allows the camera sufficient time to capture the entire experiment. The camera setting provides a reasonable resolution of 420 × 290. The camera is positioned 900 mm away from the center of the combustion chamber same as the distance between the camera and the calibration source.

4. Results and discussion

4.1. Temperature comparisons

Experiments are conducted at four different oxidizer mass fluxes of 5.91, 9.58, 18.59 and 22.19 $kg/m^2 - s$. Figures 8 and 9 are representative images using the high-speed camera for $G = 5.91$ and 22.19 $kg/m^2 - s$, respectively.

As the oxidizer flux is increased, the fuel regresses faster which is evident from the time scales in Figs. 8, 9. For $G = 5.91\ kg/m^2 - s$, the fuel sample does not burn completely and a small amount remains at the end of the run. For $G = 22.19\ kg/m^2 - s$, the wax sample burns completely within $5\,s$ and no trace of wax is left in the combustion chamber. For the lower G values, the flame appears thicker than that at higher G, consistent to the Schlieren based thermal boundary layer observed in [14]. Furthermore, the flame development is faster in higher oxidizer flux case as compared to the lower case. Qualitatively, the flame appears laminar for $G = 5.91\ kg/m^2 - s$ and turbulent with $G = 22.19\ kg/m^2 - s$.

The frames from high-speed video are extracted in MATLAB for processing using two-color pyrometry. Figures 10, 11 show the resulting temperatures corresponding to the snapshots in Figs. 8, 9,

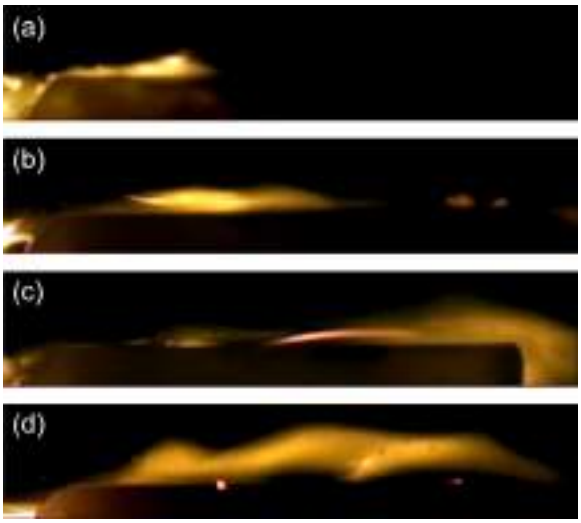

Fig. 8. Boundary layer flame over paraffin wax fuel for $G = 5.91\ kg/m^2 - s$ at different times - (a) $t = 0.2$ s, (b) $t = 0.4$ s, (c) $t = 0.6$ s, (d) $t = 2.3$ s.

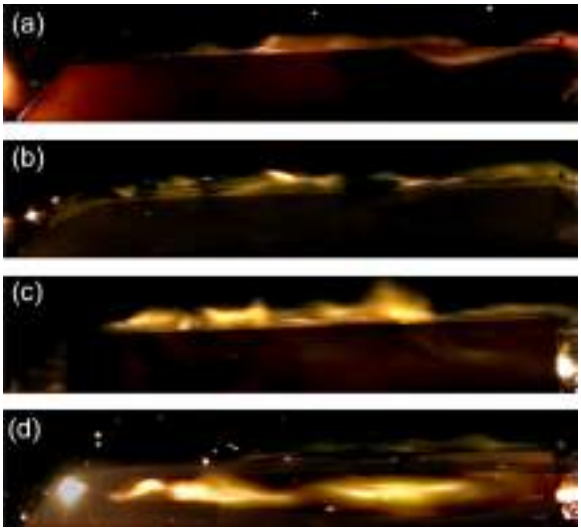

Fig. 9. Boundary layer flame over paraffin wax fuel for $G = 22.19\ kg/m^2 - s$ at different times - (a) $t = 0.5$ ms, (b) $t = 0.2$ s, (c) $t = 0.25$ s, (d) $t = 0.6$ s.

respectively. The overall temperatures are in the range of 1050 K – 3500 K, consistent to the emission spectroscopy based measurements in [23,24]. Representative wax profile is shown in the figures in green. In all the temperature contours, left of the fuel sample, a small flame is seen which corresponds to the nichrome ignition and those temperatures are neglected. The average maximum temperature for $G = 5.91\ kg/m^2 - s$ for 10 different times is 3031 K while that for $G = 22.19\ kg/m^2 - s$ is 3285 K, suggesting temperatures tend to increase with increasing G from better flow mixing. Since the intrusive temperature measurement attempts failed, the errors in two-color pyrometry measurements cannot be estimated. Nevertheless, the sensitivity of the camera sensor is characterized by estimating the error associated with ± 1 change in the digital pixel intensity and is found to be ± 7% (±175 K of the mean temperature value).

Furthermore, to check the two-color pyrometry measurements, emission spectra of the flame is also measured using an Ocean Optics HR4000 spectrometer (with a slit width of 50 μm). Figure 12 shows emission obtained at $G = 5.91\ kg/m^2 - s$. At the red and green peaks highlighted in the plot, the highest temperature of 3240 K is obtained and is consistent with the two-color pyrometry

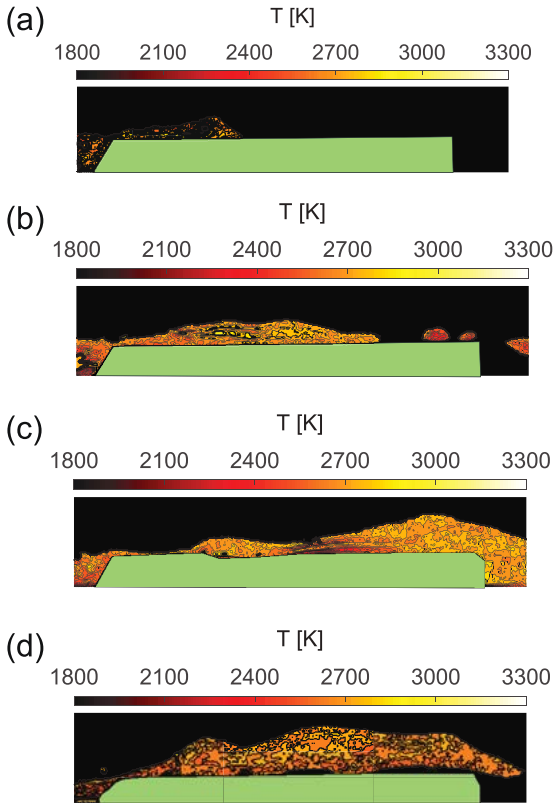

Fig. 10. Boundary layer two-color pyrometry flame temperatures over paraffin wax fuel for $G = 5.91\,\mathrm{kg/m^2} - \mathrm{s}$ at different times - (a) $t = 0.2$ s, (b) $t = 0.4$ s, (c) $t = 0.6$ s (d) $t = 2.3$ s.

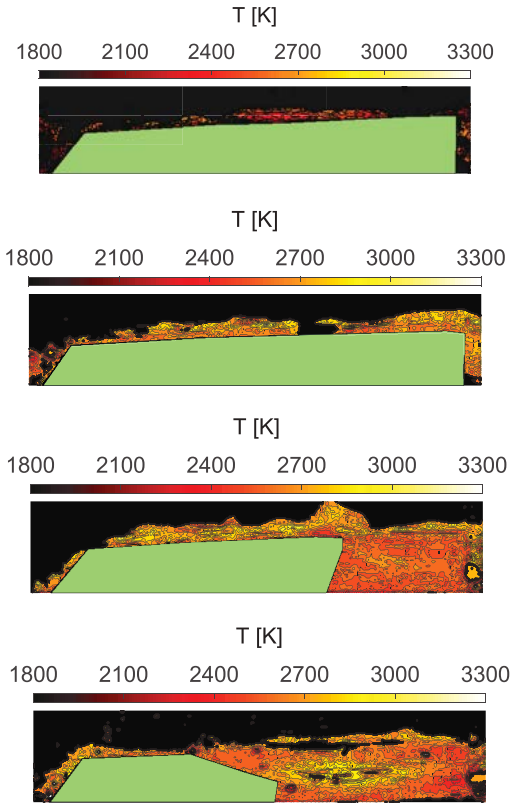

Fig. 11. Boundary layer two-color pyrometry flame temperatures over paraffin wax fuel for $G = 22.19\,\mathrm{kg/m^2} - \mathrm{s}$ at different times - (a) $t = 0.5$ ms, (b) $t = 0.2$ s, (c) $t = 0.25$ s (d) $t = 0.6$ s.

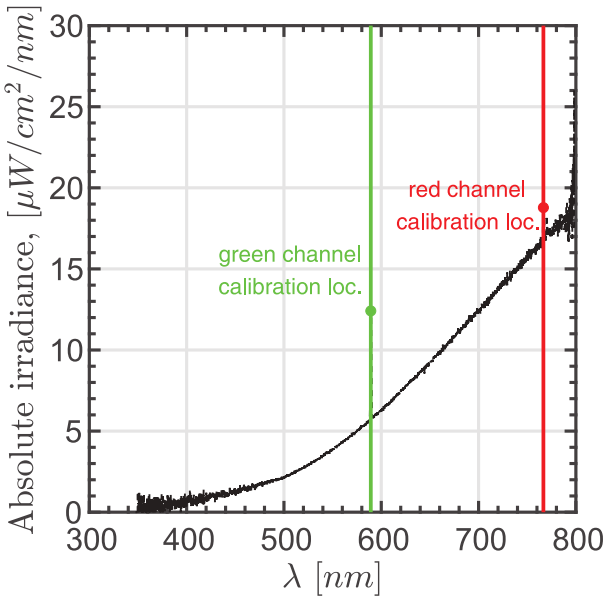

Fig. 12. Ocean Optics HR4000 spectrometer visible emission spectra for paraffin wax-oxygen combustion.

from the DSLR camera. The broadband emission spectra supports soot is the dominate source of radiation.

Figure 13 shows model predictions of the boundary layer gas temperature for (a) $G = 5.91\,\mathrm{kg/m^2} - s$ and (b) $G = 22.19\,\mathrm{kg/m^2} - s$, respectively. For each oxidizer flow rate, two cases are considered corresponding to the use of Eq. (4) for $C_f/C_{f,o}$ and the clipped version discussed in Section 2, where the blowing factor is limited to $B_* < 100$. At low oxidizer flux the boundary layer is thick as compared to that at high oxidizer flux. Also limiting C_f to reasonable values results in a high regression rate than the no clipping case resulting in a high blowing rate and therefore thicker boundary layer.

Figure 14 shows the max, min and mean temperature from the two-color pyrometry and comparison to model predictions. Only pixels which fall into the lower detection limit of the camera are used to construct statistics. The minimum temperature is therefore defined by the lower detection limit of the camera (T_{low}) that is in the range of $1000 - 1400\,\mathrm{K}$. For all the oxidizer flows, the measured mean field temperature is $\sim 2550 - 2700\,\mathrm{K}$. The maximum temperatures observed for all the four cases is between $3000\,K$ and $3400\,\mathrm{K}$ - consistent with computed adiabatic flame temperature of $3205\,\mathrm{K}$ based on using chemical equilibrium. For model comparison purposes, conditionally averaged mean temperatures are computed using $T > T_{low}$. The resulting temperatures are shown as a band in Fig. 14 and are $\simeq 100\,\mathrm{K}$ lower than the measurements - indicating very reasonable agreement. To better understand remaining differences, both K-type thermocouple and thin-filament silicon carbide fiber pyrometry measurements were attempted but both were unsuccessful due to melting of the probes. However, since the the melting temperature of silicon carbide is $3000\,K$, the measurement did indirectly confirm the gas temperatures are far higher.

4.2. Soot volume fraction

Figures 15, 16 show the soot volume fractions for $G = 5.91$ and $22.19\,\mathrm{kg/m^2} - s$, respectively, corresponding to the same images given in Figs. 10 and 11. The corresponding statistics for all oxidizer flow rates is given in Fig. 17. The general trend is the overall soot levels decrease with increasing flow rate because of the increase in turbulent mixing that promotes oxidation. In addition

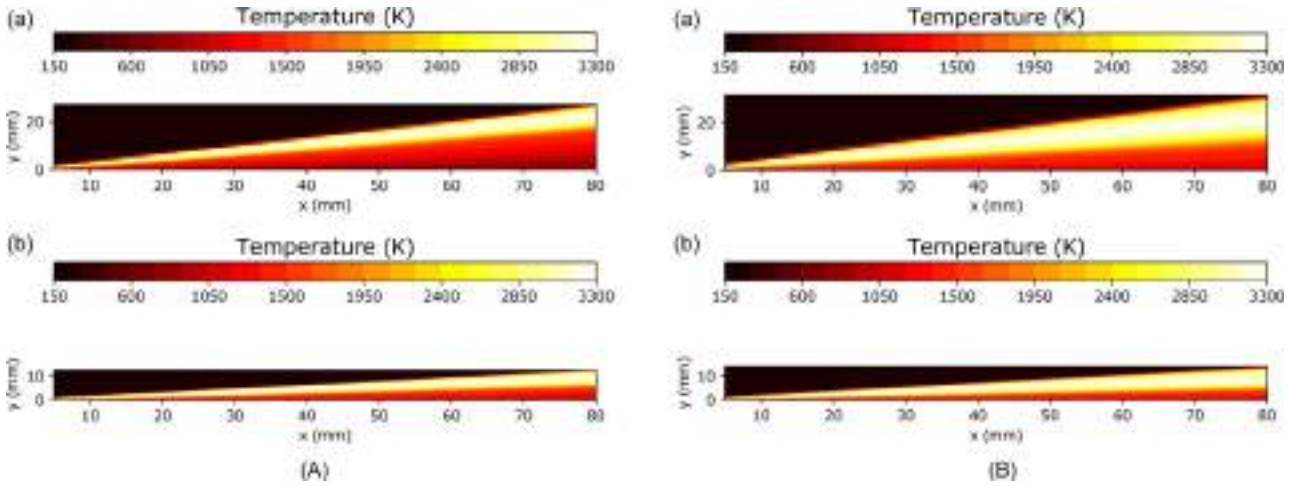

Fig. 13. Model predictions gas-phase temperature with and without clipping of Lengelle correlation for (a) $G = 5.91\,\mathrm{kg/m^2-s}$ and (b) $G = 22.19\,\mathrm{kg/m^2-s}$.

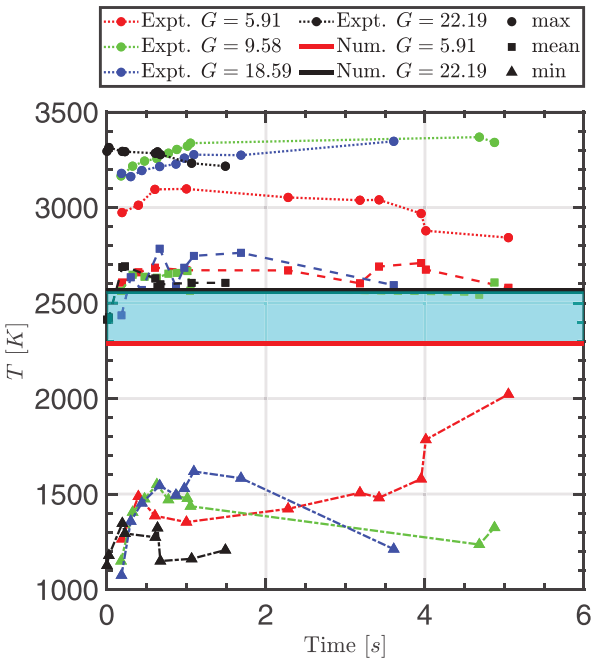

Fig. 14. Temperature statistics for four oxidizer flux (red: $5.91\,\mathrm{kg/m^2-s}$, green: $9.58\,\mathrm{kg/m^2-s}$, blue: $18.59\,\mathrm{kg/m^2-s}$, black: $22.19\,\mathrm{kg/m^2-s}$) over the experimental time.(For interpretation of the references to color in this figure legend, the reader is referred to the web version of this article.)

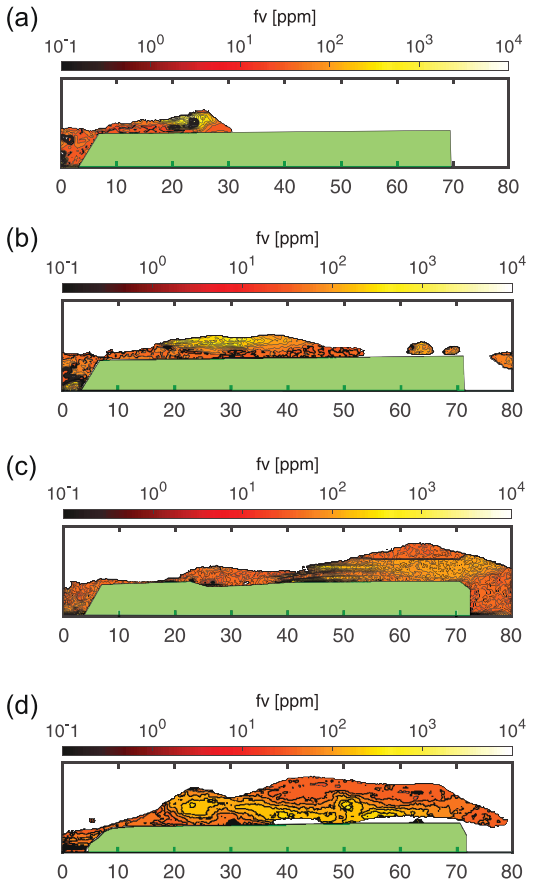

Fig. 15. Boundary layer flame soot volume fraction over paraffin wax fuel for $G = 5.91\,\mathrm{kg/m^2-s}$ at different times - (a) $t = 0.2\,\mathrm{s}$, (b) $t = 0.4\,\mathrm{s}$, (c) $t = 0.6\,\mathrm{s}$, (d) $t = 2.3\,\mathrm{s}$.

the soot levels decrease with time as the flow develops reaching a quasi-steady (statistically stationary) state. The minimum soot volume fraction ranges from 0.5 – 30 ppm and the mean soot volume fraction for all oxidizer fluxes range from 50 – 60 ppm, however, a large variation is clearly present. For the lowest oxidizer flow rate, f_v ranges between 9 – 250 ppm and for the highest flow rate, f_v ranges between 0.5 – 190 ppm. These values fall within the ranges assumed by [9].

4.3. Radiative heat flux comparisons and f_v sensitivity

To determine the radiative heat flux to the fuel surface from the experiments, a 3D flame hull is constructed similar to the technique described in [15] and assuming the cross-stream flame properties are homogeneous across the wax sample width of 1 *cm*. The flame hull from the experiments and modeling are constructed in the same manner so direct comparisons of fuel surface radiative heat flux can be compared. In both cases, gas radiation is neglected since soot is found to be the dominate emitter, and also to allow a self-consistent comparison of experiment vs. model. Figure 18 shows the radiative heat flux for (a) $G = 5.91$ and (b) $G = 22.19 - \mathrm{kg/m^2-s}$, respectively.

The peak radiative heat flux is $1.3\,\mathrm{MW/m^2}$ and $1.55\,\mathrm{MW/m^2}$ (experiment/model) for low G and $2\,\mathrm{MW/m^2}$ and $1.75\,\mathrm{MW/m^2}$ (experiment/model) for high G. Both measurements and modeling in-

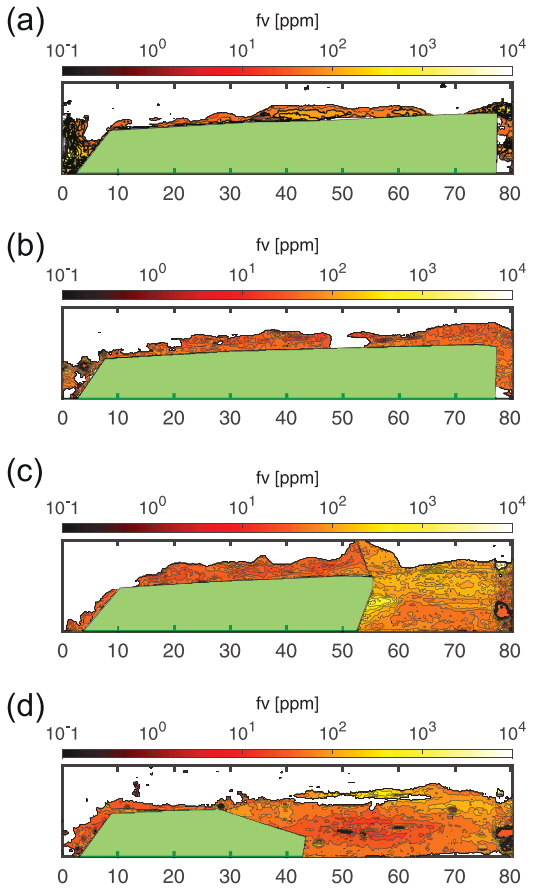

Fig. 16. Boundary layer flame soot volume fraction over paraffin wax fuel for $G = 22.19\,\mathrm{kg/m^2-s}$ at different times - (a) $t = 0.5\,\mathrm{ms}$, (b) $t = 0.2\,\mathrm{s}$, (c) $t = 0.25\,\mathrm{s}$, (d) $t = 0.6\,\mathrm{s}$.

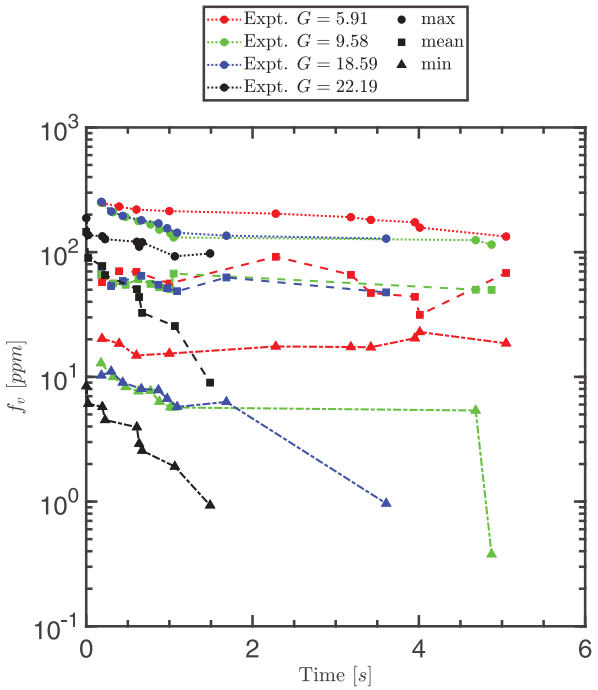

Fig. 17. Soot volume fraction statistics for four oxidizer flux (red: $5.91\,\mathrm{kg/m^2-s}$, green: $9.58\,\mathrm{kg/m^2-s}$, blue: $18.59\,\mathrm{kg/m^2-s}$, black: $22.19\,\mathrm{kg/m^2-s}$) over the experimental time. (For interpretation of the references to color in this figure legend, the reader is referred to the web version of this article.)

dicate an increase in radiative heat flux with increasing G, which initially appears counter-intuitive since f_v decreases with increasing G - indicating a decrease in the gas Plank mean absorption coefficient. This finding suggests there is a *strong feedback of the*

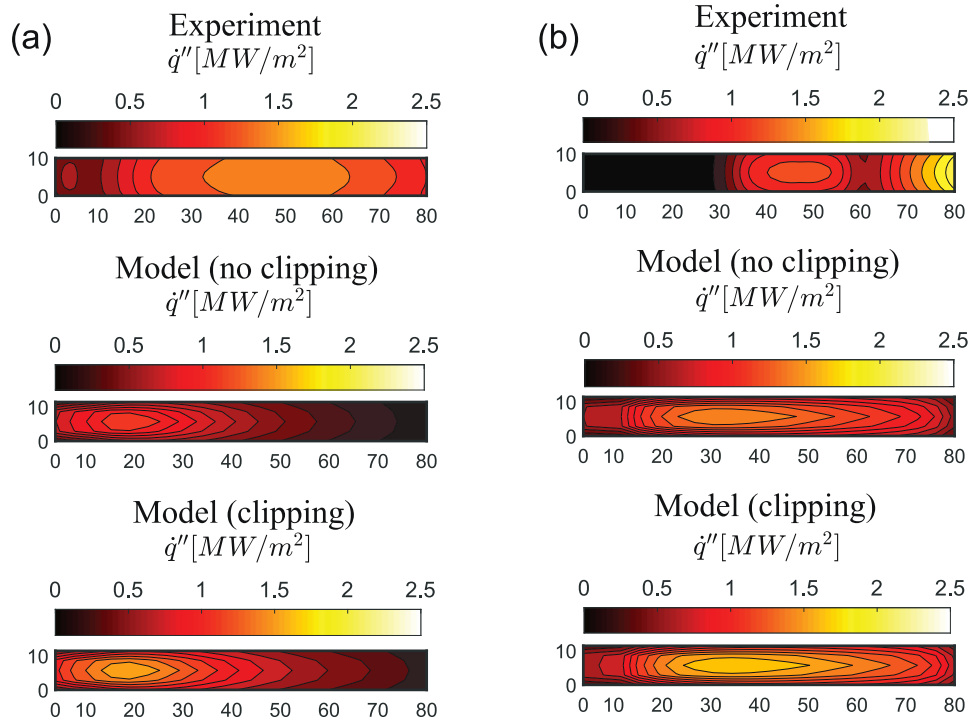

Fig. 18. Flame to fuel surface radiative heat flux feedback experimental and model (without clipping and with clipping) comparison for (a) $G = 5.91\,\mathrm{kg/m^2-s}$ and, (b) $G = 22.19\,\mathrm{kg/m^2-s}$.

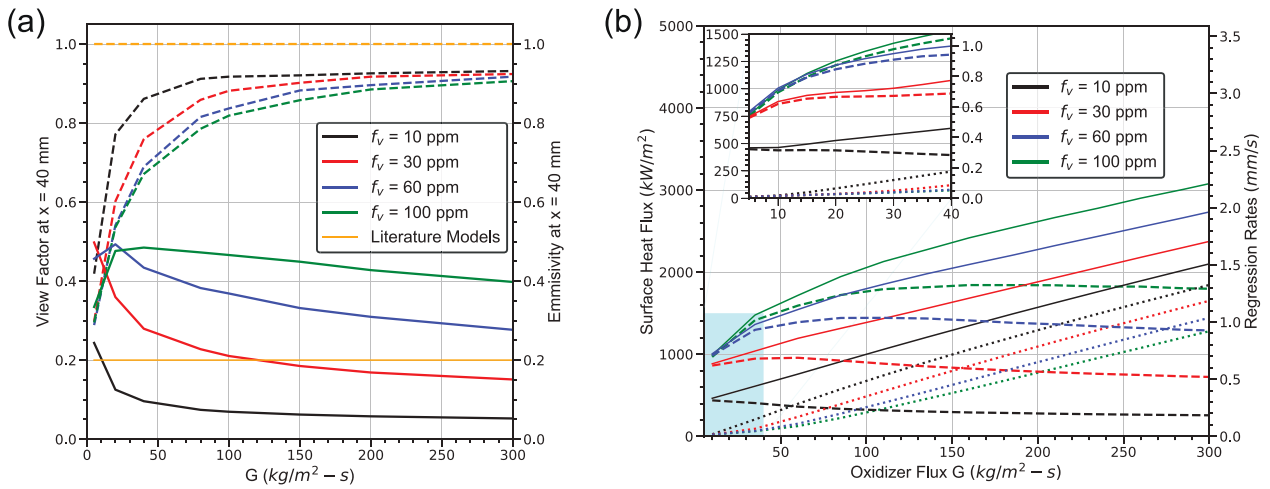

Fig. 19. Sensitivity of heat flux / regression rate to G and f_v showing (a) ϵ (solid lines) & ϕ (dashed lines) and (b) $\dot{q}''_{tot}(=\dot{q}''_{rad,inc}+\dot{q}''_g)$ (solid lines) and $\dot{r}$ (solid lines), $\dot{q}''_{rad,inc}$ (dashed lines) and $\dot{q}''_g$ (dotted lines). Blue highlighted region in (b) corresponds to area of interest on inset figure. (For interpretation of the references to color in this figure legend, the reader is referred to the web version of this article.)

blowing on defining the radiative properties of the flame either though changing the effective flame emissivity or view factor.

To better understand this behavior, additional calculations are performed assuming $f_v = 10$, 30, 60 and 100 ppm over a range of G. Flame emissivity (ϵ - solid lines) and view factor ($\phi_{f\rightarrow dw}$ - dashed lines) are plotted at a single location in Fig. 19(a) ($x = 40$ mm - centerline). The incident radiation heat flux to the surface at this location is proportional to the product of these two quantities, i.e., $\dot{q}''_{rad,inc} = \phi_{f\rightarrow dw}\,\epsilon\sigma T_{ad}^4$ where $\epsilon \equiv \int_{2\pi} I(\hat{s})\hat{n}_w \cdot \hat{s}d\Omega/(\phi_{f\rightarrow dw}\sigma T_{ad}^4)$ and $\phi_{f\rightarrow dw}$ is the flame to wax view factor.

For large G, the flame is close to the surface and ϵ is dominated by the high temperature emission. However, for low G, the boundary layer becomes thick and $\dot{q}''_{rad,inc}$ is consequently reduced from cold soot lying in between the flame and surface. The effects of self-absorption between flame and surface results in the non-monotonic behavior of ϵ at low G. Changes in ϕ with G, however, are less complex. The view factor increases with increases in either G or f_v as the boundary layer becomes thinner and more optically thick.

Figure 19 (b) shows the resulting $\dot{q}''_{tot}(=\dot{q}''_{rad,inc}+\dot{q}''_g)$ (solid lines) and $\dot{r}$ (solid lines), $\dot{q}''_{rad,inc}$ (dashed lines) and $\dot{q}''_g$ (dotted lines). A local maximum in $\dot{q}''_{rad,inc}$ is observed for $f_v = 30$, 60 and 100 ppm cases corresponding to $G = 50$, 100 and 175 kg/m$^2 - s$, respectively, due to the opposing trends in ϕ and ϵ. The relative magnitudes of radiative vs. convective heat fluxes are compared and found equal for $G = 60$, 155 and 270 kg/m$^2 - s$ for $f_v = 10$, 30 and 60 ppm, respectively, indicating that the effects of radiation cannot be easily ignored, even at relatively large oxidizer flow rates. Previous modeling studies based on Marxman theory for HTPB assume $\phi = 1$ (shown in Fig. 19(a)) and $\epsilon \simeq 0.2$ [8]. These assumptions are not supported by the current results and will lead to errors in predicted regression rates, to be discussed next.

4.4. Regression rate comparison

Time and space averaged regression rates from the experiments are compared to model predictions in Fig. 20. The blue and green dashed lines are regression rates obtained by Weinstein et al. and Karabeyoglu et al., respectively [26,27]. Experimentally obtained regression rates are shown with their associated error bars. Multiple tests are conducted to check the repeatability of the calculated regression rates and the values are found to be within 15% for $G = 5.91$ kg/m$^2 - s$ and within 7% for $G = 22.19$ kg/m$^2 - s$. Model

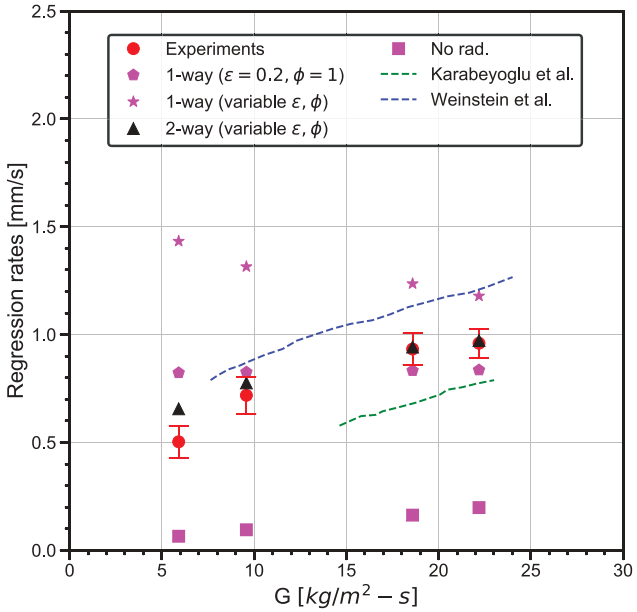

Fig. 20. Space and time averaged regression rate comparison for current experiments and numerical model (with and without clipping).

predictions are presented using various approximations of radiation heat transfer. For reference, a case without radiation is also added. As expected, excluding radiation results in significant under prediction of regression rates. The case "1-way" refers to one-way coupling using modified Marxman theory using the blowing relation of Eq. (15), however, the effects of boundary layer growth on ϵ and ϕ are ignored. In this limit, two cases are considered. In the first, ϵ and ϕ are determined from the detailed radiation solver (variable ϵ, ϕ). In the second, ϵ and ϕ are assumed constant and equal to 0.2 and 1.0, respectively, consistent with prior studies. As shown, significant over prediction of regression rates are observed using variable ϵ, ϕ. However, if these errors are compensated for using a simplified model of radiation heat transfer assuming $\epsilon = 0.2$ and $\phi = 1$ then the level of agreement to the data improves - indicating a fortuitous cancellation of errors. The last case, is the tightly coupled 2-way formulation presented in this study, using ϵ and ϕ properties from the detailed radiation solver.

For this case, the level of agreement with data appears quite good and suggests that incorporating detailed descriptions of radiation heat transfer results in improved agreement.

5. Conclusions

In this study, the theory of Marxman et al. is expanded on for including the effects of radiation heat transfer. A general relation is derived to account for the intimate coupling of surface blowing with descriptions of changes in skin friction. This relation provides a framework for obtaining physically realizable estimates of C_f when effects of radiation are incorporated. The extended Marxman model is tightly coupled to a DTM solver of soot radiation heat transfer so additional blowing from radiation heat transfer will directly affect flame emissivity and view factor. Slab burner experiments are conducted to test the limitations of the modeling approach. Measurements of regression rates, soot volume fraction, and radiation heat flux to the fuel surface are carried out using DSLR camera two-color pyrometry and approximate flame hull reconstruction. Overall model comparisons to experimental measurements of radiative heat flux and regression rates are shown to be reasonable. Model sensitivity studies reveal commonly used 1-way coupling strategies may result in significant over prediction in fuel regression rate that are most likely compensated for by errors in simplified treatments of radiation heat transfer.

Declaration of Competing Interest

The authors declare that they have no known competing financial interests or personal relationships that could have appeared to influence the work reported in this paper.

The authors declare the following financial interests/personal relationships which may be considered as potential competing interests:

Acknowledgment

Support has been provided in part by National Science Foundation (NSF) under grant number #1704447 and the NASA microgravity program under grant number 80NSSC20K0426.

Appendix A. Solution algorithm and heat transfer validation

This appendix summarizes the two eigenvalue solution approaches with incorporating unsteady heat transfer and radiation heat transfer. To validate the numerical heat transfer model with moving boundaries, a Stefan freezing problem is solved and compared to exact analytical solutions.

A1. Solution Algorithm

1. Guess Value of Surface Radiative heat flux.
2. (a) Guess value of $Y_{f,s}$ and determine T_s from Antoine vapor pressure relation.

(b) Determine blowing parameter, B_*, using $h-ox$ coupling function given in Eq. (12) where $\dot{q}''_{l,lg}$ determined from the time dependent numerical simulation.

(c) Re-compute $Y_{f,s}$ using B_* expressed in terms of $f-ox$ coupling function, $Y_{f,s}=(B_*-Y_{ox,e}/\nu_{ox})/(1+B_*)$

(d) Iterate until convergence using bi-sectional based algorithm since the bounds of $Y_{f,s}$ are known.

(e) Compute $\dot{q}''_{g,s}$ using Eq. (7).

3. Compute $\dot{q}''_{rad}$ from new gas phase solution, and iterate until convergence is reached.

Solving for the next time step is done in three steps.

1. Solve for the heat flux and temperature at the liquid-gas surface using the iterative model above with $\dot{q}''_{l,lg}$ taken at the current time step.
2. Use Eqs. (23), (24) to move the interfaces using a forward Euler Method.
3. Solve the convection-diffusion problems in both the liquid and solid phases and update the time.

A2. Validation of numerical heat transfer model

To check the numerical model, cases are conducted for the Stefan freezing problem where the following exact solution is available,

$$T^*(y^*,\tau)=\begin{cases}\frac{erf(\frac{y^*}{2\sqrt{\tau}})}{erf(\lambda\sqrt{\frac{\alpha_l}{\alpha_s}})} & 0\le y^*\le R(t)\\ \frac{T_l-T_s}{T_m-Ts}-\frac{T_l-T_m}{T_m-T_s}\frac{erfc(\sqrt{\frac{\alpha_s}{\alpha_l}}\frac{y^*}{2\sqrt{\tau}})}{erfc(\lambda)} & R(t)\le y^*\end{cases} \tag{A.1}$$

where $T^*=\frac{T-T_s}{T_m-T_s}$ is the non-dimensional temperature, $\tau=t\alpha_s/L^2$ is the non-dimensional time, $y^*=y/L$ is the non-dimensional length away from a surface held at temperature $T_s<T_m$ where T_m is the freezing temperature, $R(t)=r(t)/L$ is the non dimensional freezing interface a distance $r(t)$ away from the surface, and $T_l>T_m$ is the initial temperature of the liquid. The density is assumed constant and equal in the liquid and solid phases, and the thermal properties for the liquid and solid are assumed not to depend on the temperature and are constant throughout each phase. Figure A.1a shows representative modeling results compared to the exact solution at non-dimensional times of $\tau=0.11, 1.06, 10.58$. Figure A.1b shows the rate of convergence at $\tau=0.31$ showing second order spatial error convergence.

To further test the numerical heat transfer model, regression rates are compared to the analytical solution of Karabeyoglu et al. The analytical solution assumes equal regression rates for the liquid-gas ($\dot{r}_{lg}$) and liquid-solid ($\dot{r}_{ls}$) interfaces. A closed form solution to the Stefan problem may therefore be determined,

$$T(y)=\frac{[1-\exp(y/\Gamma_l)]T_s+[\exp(y/\Gamma_l)-\exp(h/\Gamma_l)]T_m}{1-\exp(h/\Gamma)} \tag{A.2}$$

where T_m is the melting temperature of the paraffin, $\Gamma_l\equiv\alpha_l/\dot{r}$ is the characteristic thermal thickness and α_l is the liquid thermal diffusivity. The resulting (downward) conduction heat flux at any location through the liquid is given as:

$$\dot{q}''_l(y)=k_l\frac{\partial T}{\partial y}=\dot{m}''C_l\left[T(y)-\frac{T_s-T_m\exp(h/\Gamma_l)}{1-\exp(h/\Gamma_l)}\right] \tag{A.3}$$

therefore the difference in heat flux entering and existing the liquid layer is:

$$\Delta\dot{q}''=\dot{q}''_{l,lg}-\dot{q}''_{l,ls}=\dot{m}''C_l(T_s-T_m) \tag{A.4}$$

showing the exiting heat conduction is reduced due to upward convection. Substituting this result into the energy balance at the $l-s$ interface, then $\dot{q}''_{l,lg}$ can be directly related to the heat flux entering the solid, $\dot{q}''_s$.

$$\dot{q}''_{l,lg}=\dot{q}''_{l,ls}+\dot{m}''C_l(T_s-T_m)=\dot{q}''_s+\dot{m}''(L_m+C_l(T_s-T_m)) \tag{A.5}$$

where L_m is the latent heat of melting and $\dot{q}''_s$ is the heat entering the solid phase that is approximated using a modified semi-infinite media approximation,

$$\dot{q}''_s=\begin{cases}0 & \text{for } t<\tau_m\\ \frac{k_s(T_m-T_\infty)}{\sqrt{\pi\alpha_s(t-\tau_m)}} & \text{otherwise}\end{cases} \tag{A.6}$$

where $\tau_m=\frac{1}{4}\pi k_s\rho_s C_s[(T_m-T_\infty)/\dot{q}''_{g,ad}]^2$ is a time for the surface to reaching the melting temperature - assuming an adiabatic surface,

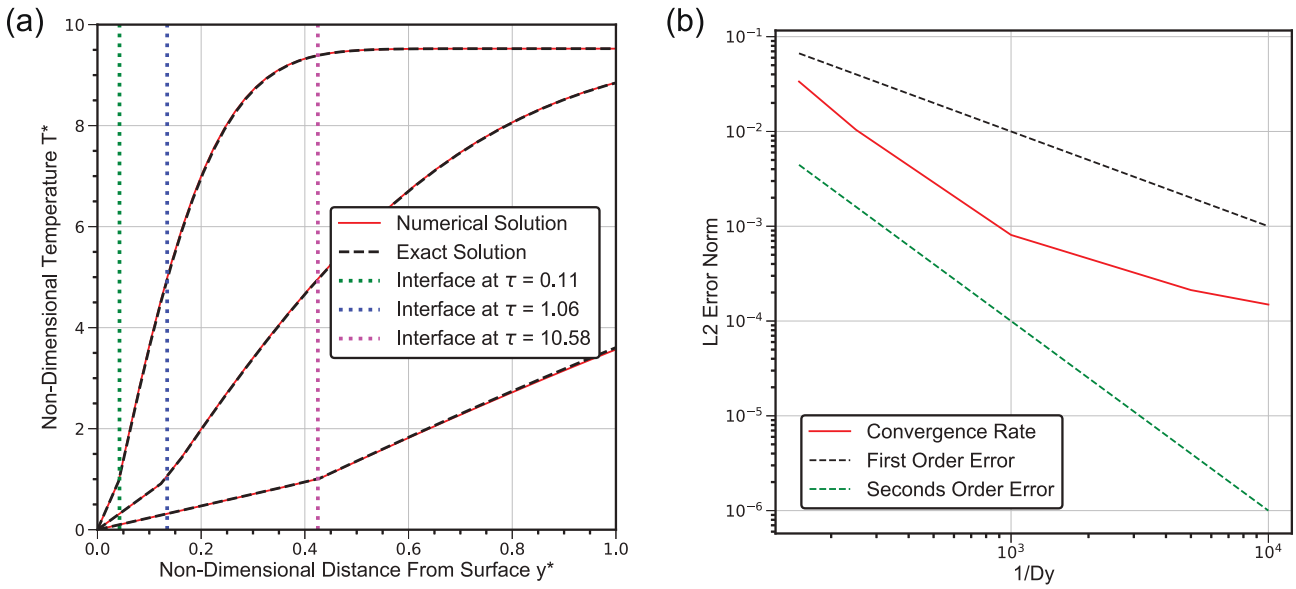

Fig. A.1. Summary of Stefan freezing problem results showing (a) comparison of numerical result with exact solution at $\tau = 0.11, 1.06,$ and 10.58 and (b) spatial error convergence. For these cases, the density is assumed uniform and thermal properties constant in their respected phases.

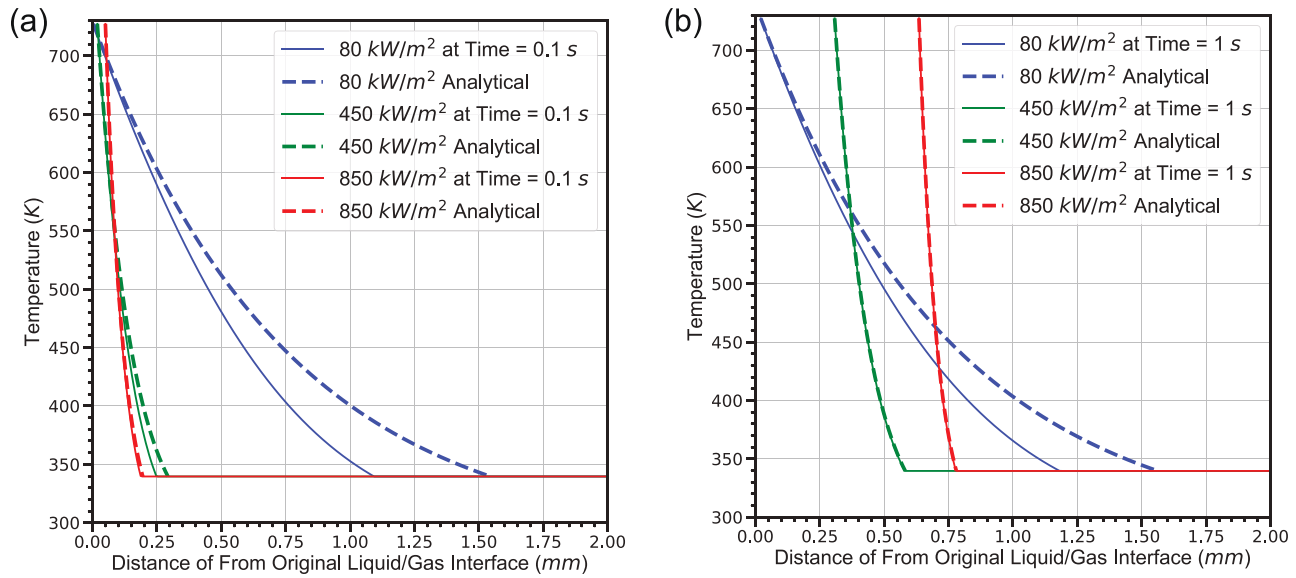

Fig. A.2. Liquid layer Temperature distribution for prescribed surface heat fluxes using the analytical steady solution and numerical unsteady solution evaluated at (a) 0.1 s and (b) 1 s.

Eq. (19). Figure A.2 compares numerical (solid lines) and analytical (dashed lines) solutions through the liquid wax layer. Solutions are obtained for heat flux values of 80, 450 and 850 $\mathrm{kW/m^2}$ after 0.1 and 1 s. The initial condition is $T(x, t = 0) = T_m$ where T_m is the wax melting temperature. For high heat fluxes steady state solution is reached very quickly and the numerical and analytical solutions are identical. For low heat fluxes differences are apparent because of the equal $\dot{r}$ assumption used in the analytics. For the radiation cases, surface heat fluxes are in excess of 850 $\mathrm{kW/m^2}$ therefore either analytical or numerical solution approaches would work fine. However, cases ignoring radiation heat flux values are $80 - 140\,\mathrm{kW/m^2}$ and therefore numerical solution approaches are necessary.

References

[1] X. Sun, H. Tian, Y. Li, N. Yu, G. Cai, Regression rate behaviors of HTPB-based propellant combinations for hybrid rocket motor, Acta Astronaut. 119 (2016) 137–146.

[2] Y. Komori, K. Takahashi, I. Nakagawa, Combustion characteristics of adding micro-sized aluminum powder to wax-based hybrid rocket fuel by using axial and swirl flow, 53rd AIAA/SAE/ASEE Joint Propulsion Conference (2017), p. 4644.

[3] V.I. Naoumov, N.A. Al Masoud, K. Sherman, M. Doolittle, M. Ziegler, D. Thorne, Study of the combustion of pure bio-derived fuels and bio-derived fuels with additives in hybrid propellant rocket engine, 55th AIAA Aerospace Sciences Meeting (2017), p. 0833.

[4] K.K. Kuo, M.J. Chiaverini, Fundamentals of hybrid rocket combustion and propulsion, American Institute of Aeronautics and Astronautics, 2007.

[5] G.A. Marxman, M. Gilbert, Turbulent boundary layer combustion in the hybrid rocket, Symp. (Int.) Combust. 9 (1963) 371–383.

[6] G.A. Marxman, C.E. Wooldrige, R.I. Muzzy, Fundamentals of hybrid boundary layer combustion, Prog. Astronaut. Aeronaut. 15 (1964) 485–522.

[7] G.A. Marxman, Combustion in the turbulent boundary layer on a vaporizing surface, Symp. (Int.) Combust 10 (1965) 1337–1349.

[8] M.J. Chiaverini, K.K. Kuo, A. Peretz, G.C. Harting, Regression-rate and heat–transfer correlations for hybrid rocket combustion, J. Propuls. Power 17 (1) (2001) 99–110.

[9] G. Leccese, D. Bianchi, F. Nasuti, K.J. Stober, P. Narsai, B.J. Cantwell, Experimental and numerical methods for radiative wall heat flux predictions in paraffin based hybrid rocket engines, Acta Astronaut. 158 (2019) 304–312.

[10] G. Leccese, D. Bianchi, F. Nasuti, K.J. Stober, P. Narsai, B.J. Cantwell, Experimental and numerical evaluation of the radiative wall heat flux in the post

chamber of a paraffin based hybrid rocket engine, 7th European Conference for Aeronautics and Aerospace Sciences (2017) 149 (2017).
[11] L. Strand, M. Jones, R. Ray, N. Cohen, Characterization of hybrid rocket internal heat flux and HTPB fuel pyrolysis, 30th Joint Propulsion Conference and Exhibit (1994), p. 2876.
[12] Y. Funami, T. Shimada, Numerical evaluation of hybrid rocket internal ballistics with thermal radiation effect, T. Jpn. Soc. Aeronaut. S., Aero. Tech. Jpn. 12 (2014) 21–30.
[13] J.-E. Durand, F. Raynaud, J.-M. Lamet, L. Tessé, J.-Y. Lestrade, J. Anthoine, Numerical study of fuel regression in hybrid rocket engine, 54th Joint Propulsion Conference (2018), p. 4593.
[14] C. Dunn, G. Gustafson, J. Edwards, T. Dunbrack, C. Johansen, Spatially and temporally resolved regression rate measurements for the combustion of paraffin wax for hybrid rocket motor applications, Aerosp. Sci. Technol. 72 (2018) 371–379.
[15] S.S. Aphale, P.E. DesJardin, Development of a non-intrusive radiative heat flux measurement for upward flame spread using DSLR camera based two-color pyrometry, Combust. Flame 210 (2019) 262–278.
[16] G. Lengelle, Model describing the erosive combustion and velocity response of composite propellants, AIAA J. 13 (3) (1975) 315–322.
[17] A.M. Karabeyoglu, Transient Combustion in Hybrid Rockets, Stanford University, 1998 Ph.D. thesis.
[18] D. Drysdale, An introduction to fire dynamics, John Wiley and Sons, New York, NY, 1998.
[19] A. Kudchadker, B. Zwolinski, Vapor pressure and boiling points of normal alkanes, C21 to C100., J. Chem. Eng. Data 11 (2) (1966) 253–255.
[20] F. Lockwood, N. Shah, A new radiation solution method for incorporation in general combustion prediction procedures, Symp. (Int.) Combust., 18, Elsevier (1981), pp. 1405–1414.
[21] B. Leckner, Spectral and total emissivity of water vapor and carbon dioxide, Combust. Flame 19 (1) (1972) 33–48.
[22] M.F. Modest, Radiative heat transfer, McGraw-Hill, 1993.
[23] K.J. Stober, G. Leccese, P. Narsai, K. Ozawa, B.J. Cantwell, Flame emission spectroscopy in a paraffin-based hybrid rocket, 67th International Astonautical Congress (IAC), 2016a, p. 8.
[24] K.J. Stober, P. Narsai, K. Venkataraman, A. Thomas, B.J. Cantwell, Flame emission spectroscopy in a paraffin-based hybrid rocket, 52nd AIAA/SAE/ASEE Joint Propulsion Conference (2016b), p. 4564.
[25] P.B. Kuhn, B. Ma, B.C. Connelly, M.D. Smooke, M.B. Long, Soot and thin-filament pyrometry using a color digital camera, Proc. Combust. Inst. 33 (1) (2011) 743–750.
[26] A. Weinstein, A. Gany, Testing and modeling liquefying fuel combustion in hybrid propulsion, Prog. Propuls. Phys. 4 (2013) 99–112.
[27] M. Karabeyoglu, B. Cantwell, D. Altman, Development and testing of paraffin-based hybrid rocket fuels, 37th Joint Propulsion Conference and Exhibit (2001), p. 4503.